

Article

A Novel Approach of Slope Detection Combined with Lv's Distribution for Airborne SAR Imagery of Fast Moving Targets

Yuefeng Zhao, Shengliang Han * , Jimin Yang, Liren Zhang, Huaqiang Xu and Jingjing Wang *

School of Physics and Electronics, Shandong Normal University, Jinan 250000, China;
yuefengzhao@126.com (Y.Z.); jmyang@sdnu.edu.cn (J.Y.); zhangliren66@hotmail.com (L.Z.);
xuhq@sdnu.edu.cn (H.X.)

* Correspondence: hansehngliang@hotmail.com (S.H.); wjj@sdnu.edu.cn (J.W.); Tel.: +151-0541-0857 (S.H.)

Received: 30 March 2018; Accepted: 13 May 2018; Published: 15 May 2018



Abstract: This paper presents a fast SAR imagery algorithm for Ground Moving Target Imaging (GMTIm) based on the slope detection strategy combined with Time-Frequency Representation (TFR), which is known as Lv's Distribution (LVD). This fast imagery algorithm focuses on the solution of the ambiguity problems and relevant heavy computing load in SAR imagery. Firstly, according to the relationship between the slope of the range walk trajectory and the cross-track velocity of moving target, a new high-efficiency slope detection strategy based on gradient and level-line angle is presented in the image domain. Then, the Doppler centroid shift induced by cross-track velocity can also be obtained. Secondly, owing to the cross-track velocity estimated before, the Range Walk Migration Correction (RWMC) can be performed to concentrate the echo response of the moving target into a single range cell. Finally, due to the superior performance in representing multi-component Linear Frequency Modulation (LFM) signal, LVD is adopted here to represent the Doppler chirp rate of multiple moving targets in a Doppler Centroid Frequency and Chirp Rate domain (CFCR). The performance of the proposed algorithm is evaluated in terms of superiority and effectiveness using simulations, and the comparison between the proposed algorithm and the other conventional algorithms is also presented.

Keywords: ground moving target imaging (GMTIm); Airborne Synthetic Aperture Radar; slope detection; lv's distribution (LVD)

1. Introduction

Airborne Synthetic Aperture Radar (SAR) has the capability of remote sensing regardless the weather conditions and indifferently in day and night. Furthermore, the development of radar signal processing technology has provided it with the capability of imaging and positioning of ground moving targets, so that SAR has tracked even more attentions in both civilian and military applications [1–9]. Generally, in order to achieve a high azimuth resolution, the SAR system adopts the synthetic aperture technique by installing radar sensor on aerial platforms, which is required to fly on a fixed routine [10]. The SAR sensor monitors ground moving targets by transmitting a large number of broadband pulses, so the reflected pulses is related to the motion parameters, which makes the moving targets unfocused and smeared in SAR images [2]. Furthermore, the cross-track (radial) and the along-track velocity are the main reasons leading to Doppler parameter variation and large range migration, which influence the accuracy of velocity estimation as well as the radar imaging quality. Obviously, this is a challenge for fast moving target imaging [5,11–19]. Specifically, comparing stationary targets, the cross-track velocity of moving targets causes the Doppler centroid shift and the extra range walk migration, whereas the along-track velocity has an effect on the Doppler modulation rate [20,21].

To address this issue, Ground Moving Target Imaging (GMTIm) is developed to enhance the capability of image formation and parameters estimation for airborne SAR. Existing GMTIm algorithms can be classified into two categories: single channel and multiple channel algorithms. Multiple channel algorithms utilize the interferometric phase between different SAR channels to resolve the ambiguity problem related to the target motion parameters. The algorithms, such as Along-Track Interferometry (ATI) [22], Displaced Center Antenna (DPCA) [23,24] and Space-Time Adaptive Processing (STAP) [25,26] are capable of moving target focusing and precise motion parameter acquiring [2,10,27–30]. However, these multiple channel SAR algorithms usually suffer from both expensive computing costs and complicated equipment installation. In addition, the susceptible registration error also has a significant effect on the radar signal processing [31]. Therefore, the research of imagery algorithm for single channel SAR is still opening.

For single channel SAR imagery algorithms, as aforementioned, one of the core procedure is the Range Walk Migration Correction (RWMC). The main methods to remove range walk migration can be divided into two sorts. First, as a classical means, by rescaling the slow time axis to remove the coupling between range frequency and slow time, Keystone Transform (KT) is an effective tool to correct the range walk migration without knowing the motion parameters of moving targets [5,6,32–36]. Besides, owing to the significant performance in correcting a large range curve migration or the quadratic component of the range migration, the second-order KT is also widely used in many applications to eliminate the effects of range curve migration [33]. However, in the case of the fast moving target, the problem of Doppler ambiguity must be take into consideration for the application of KT, which in turn increases the computational complexity. Additionally, all the relative KT-based methods are subjected to a large computational load caused by the interpolation operation [36]. To reduce the computational load is still a challenge for KT. Second, for RWMC, the cross-track velocity is the most interesting motion parameter of the moving target. Considering the relationship between the slope of the range walk trajectory and cross-track velocity, Randon Transform (RT) and Hough Transform (HT) are used to obtain the slope of the range walk trajectory [1,37–43]. Both the above two algorithms can get rid of the limitation of the Doppler ambiguity and the cross-track velocity can be well estimated simultaneously. However, due to the searching angles and ranges to obtain a high precision value of the slope, both RT and HT suffer from a large computational load [36]. Although HT is efficient, it is subjected to a high signal-to-noise ratio. In addition, the drawback that the computing time increases with the number of targets existed in the observed scene also has an effect on the applications of HT. So that when these two methods are used in the SAR signal processing, the tradeoff between estimation precision and computational load has to be well deliberated, especially for a real-time SAR system.

After range compression, range curve and range walk migration correction, the energy of moving target is concentrated into a single range cell, and the Doppler parameters with related to along-track velocity can be obtained within the range cell. Since the Azimuth Phase Modulation (APM) is in a linear frequency modulated form, the time-frequency analysis is widely adopted in GMTIm algorithms, such as Wigner-Ville Distribution (WVD) [44] and Fractional Fourier Transform (FrFT) [45]. In practice, where multiple moving targets are closely located in the observe scene, a multi-component LFM echo will appear. In addition, the WVD-based methods are limited by its cross-terms and cannot be regarded as the real characteristic of the LFM signal [10]. Although FrFT can get rid of the influence of cross-terms, but it still cannot get a real representation of the modulate rate [46].

To tackle these issues in the aforementioned methods, in this paper, a novel imaging algorithm based on the Slope Detection strategy combined with LVD (SDLVD) is proposed to obtain a high quality SAR image and precise motion parameters. In order to facilitate the analysis and conclusion, a general SAR geometry was adopted here. Then, based on the principle of gradient and level-line angle [47], an efficient and accurate slope estimation method is applied into estimating the target trajectory slope and correcting the range walk migration. Next, due to the advantageous performance in representing multiple moving targets in a Doppler Centroid Frequency and Chirp Rate (CFCR) domain, LVD is used

to obtain the Doppler modulate rate of the moving target [10,46,48–51], meanwhile, the along-track velocity can also be calculated. After the azimuth compression, the final image of moving target can be well focused. In the end, simulation results are exhibited for the certification of the proposed algorithm.

The rest of the paper is organized as follows. Section 2 presents a universal radar-moving target geometry, and the analysis of echo signal characteristics is also given. Section 3 presents a novel slope estimation method and LVD is also used to acquire the along-track velocity. Section 4 focuses on the performance evaluation for the proposed algorithms in terms of the effectiveness and accuracy. Finally, conclusions are presented in Section 5.

2. Airborne SAR Echo Signal Model and Analysis

This section presents a single channel SAR geometry, where all targets are supposed to be isotropic points in the geometry and a ground moving target M is modeled with a constant velocity, meanwhile a stationary target S is constructed to represent the static ground or the target. Following the conventional research approach, the SAR geometry is assumed to be a linear system, which makes the echo signal as the linear accumulation of the targets. Besides, the intended algorithm is focused on the fast-moving target velocity parameters estimations, which involves severe range walk migration. Taylor's series approximation and far-field hypothesis are also utilized in the analysis of the echo signal model.

2.1. SAR Geometry of Fast Moving Target

The geometry model of a single-channel strip-map mode SAR system is shown in Figure 1a. A spatial Cartesian coordinate system is used to depict the geometry, whereas S represents a stationary target and M denotes a moving target with cross-track velocity V_y and along-track velocity V_x . The SAR sensor flights at the height of H , v_a is the forward velocity of the platform while t_a is the flight time of the platform, also known as slow time. R_0 and $R_{(t_a)}$ denote the nearest and the instantaneous slant ranges of the target, respectively. Similarly, X represents the nearest ground range of the target. The instantaneous coordinates of the platform and the moving target can be defined as $(V_a t_a, 0, H)$ and $(X + V_x t_a, Y + V_y t_a, 0)$.

As aforementioned depiction, under the hypothesis that the platform flies along the predetermined trajectory, the distance between the moving target and the radar is dynamic. As shown in Figure 1a, $R_{(t_a)}$ can be given as

$$R_{(t_a)} = \sqrt{(V_a t_a - X - V_x t_a)^2 + (Y + V_y t_a)^2 + H^2} \quad (1)$$

Apply the third-order Taylor series coefficients expansion into Equation (1), $R_{(t_a)}$ can be simplified as

$$R_{(t_a)} \approx R_0 + \frac{Y V_y}{R_0} t_a + \frac{(v_a - v_x)^2}{2R_0} t_a^2 - \frac{Y V_y (v_a - v_x)^2}{2R_0^3} t_a^3 \quad (2)$$

It can be seen that the cubic component of Equation (2) is proportional to the cross-track velocity V_y , and this component cannot be ignored in the further analysis, especially for the fast-moving target. Integrating Equation (2) into the SAR geometry on a slant range plane as shown in Figure 1b, V_r represents the radial velocity, which is related to the cross-track velocity V_y . According to the projection relationship of the motion parameters between the range domain and slant range domain [43], The instantaneous slant range with relation to the radial velocity can be expressed as

$$R_{(t_a)} \approx R_0 + V_r t_a + \frac{(v_a - v_x)^2}{2R_0} t_a^2 - \frac{V_r (v_a - v_x)^2}{2R_0^2} t_a^3 \quad (3)$$

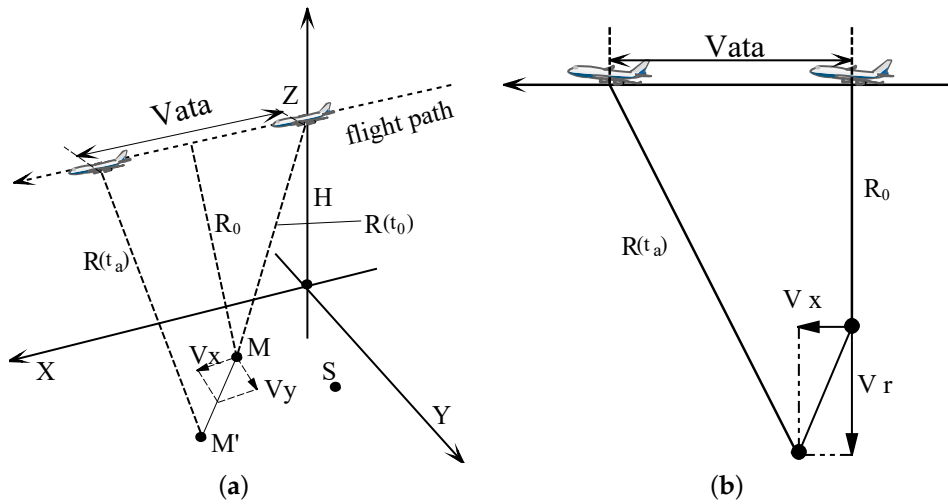


Figure 1. Broadside geometry of a moving target and a static target in the single-channel SAR system: (a) geometry in a Cartesian coordinate system; (b) geometry on a slant range plane.

Assuming that the SAR sensor transmits a LFM signal with the carrier frequency f_c

$$s(\hat{t}, t_a) = w_r(\hat{t}) \exp(j2\pi f_c t_a) \quad (4)$$

where \hat{t} represents the signal propagation time, also known as fast time, and $w_r(\hat{t})$ is the window of the LFM signal. In the analysis of the echo signal, assuming that λ is the wavelength of the transmit signal and c is the speed of light, After range compression the receiving signal can be shown as

$$s(\hat{t}, t_a) = A w_a(t_a) \text{sinc}[\pi B(\hat{t} - \frac{2R(t_a)}{c})] \exp[-j\frac{4\pi}{\lambda} R(t_a)] \quad (5)$$

where A defines the backscatter coefficient, $w_a(t_a)$ represents the azimuth window, B is the bandwidth of the transmitted signal. By substituting (3) into (5) and taking FFT with respect to the fast time, the echo signal can be constructed as:

$$s(f_r, t_a) = A w_a(t_a) W(f_r) \exp(-j\frac{4\pi}{\lambda} R_0) \exp(-j\frac{4\pi}{\lambda} V_r t_a) \exp(-j\frac{4\pi R_0}{c} f_r) \exp(-j\frac{4\pi V_r}{c} f_r t_a) \exp(j\frac{4\pi}{\lambda} \frac{V_r (V_a - V_x)^2}{2R_0^2} t_a^3) \exp(-j\frac{4\pi}{c} \frac{(V_a - V_x)^2}{2R_0} f_r t_a^2) \exp(-j\frac{4\pi}{\lambda} \frac{(V_a - V_x)^2}{2R_0} t_a^2) \quad (6)$$

where f_r is the range frequency and $W(f_r)$ denotes the envelope of the range frequency spectrum.

2.2. Motion Parameters Analysis

In Equation (6), it can be drawn that the spectral information is exhibited in the range-frequency and azimuth-time domain with seven exponential terms. The first and the fifth exponential terms have no virtual effect on the following analysis and will not be considered further. The second exponential term indicates that the Doppler centroid shift, $f_{dc} = 2V_r/\lambda$. The third exponential term indicates that the Doppler modulate rate of the fast moving target is mainly affected by the along-track velocity. The fourth exponential term, called Range Walk Migration (RWM), usually creates the problem of defocus and misalignment in SAR images. In contrast, the sixth exponential term, called Range curve Migration (RcM), causes the trajectory curve in the range-compressed domain. Furthermore, the combination of RWM and RcM is called Range Cell Migration (RCM), which can be expressed as

$$RCM = \exp(-j\frac{4\pi V_r}{c} f_r t_a) \exp(-j\frac{4\pi (V_a - V_x)^2}{2R_0} f_r t_a^2) \quad (7)$$

The fifth exponential term in Equation (6) is the cubic phase error of the fast-moving target, which is an important parameter, especially when V_r increases. Equations (6) and (7) show that V_r has significant influence on the echo signal spectrum. The keystone transform is usually deployed to correct the range walk migration, but it may not be a practical solution when the conundrum of Doppler ambiguity arises. From this point of view, to obtain high quality image, the range walk migration needs to be compensated accurately. Therefore, a precise estimate value is vital to form a high quality SAR image, especially for fast-moving targets.

3. Algorithm Description

3.1. RCMC and Radial Velocity Estimation

In the aforementioned analysis, the RCM of the moving target must be compensated to obtain a focused SAR image. After the range compression, due to the range curve migration, the straight line trajectory of the moving target becomes deformed. This kind of distortion can lead to a large estimation error in the detection of the slope of the trajectory, therefore, the range curve migration must be corrected ahead of the detection of the slope. Nevertheless, V_x is an unknown parameter in the seventh exponential term in Equation (6). Since the fact that the along-track velocity of moving target is much smaller than the velocity of platform, it is available for the approximation to ignore the effect of the along-track velocity. Therefore, the match-filter function for RCM correction can be approximated as follows

$$H_{RCM} \approx \exp(j\frac{4\pi V_a^2}{c} \frac{V_a^2}{2R_0} f_r t_a^2) \quad (8)$$

In addition, the effect of this kind of range curve migration correction has been validated in [1]. Once the range curve migration is corrected, the trajectory of the moving target can be focused into a straight line in the frequency-time domain. Then the relationship between the slope and the radial velocity is depicted as shown in Figure 2, which can be expressed as

$$\hat{V}_r = \frac{PRF \times \tan \hat{\theta} \times c}{2f_c} \quad (9)$$

where $\hat{\theta}$ is the estimated slope of the trajectory, PRF is the pulse repetition frequency. Actually, the key is the estimation of trajectory slope [1,40,41]. To acquire the slope from the aforementioned range-compressed and range corrected image, the image processing techniques are used. For example, HT and RT are used to obtain the slope, in which RT requires low Signal-to-Noise Ratio (SNR), but HT is more efficient than RT. Notes that all RT- and HT-based methods are required to map each point of the image into the parameter space. In this case, the computing load can be extremely heavy [31]. Such kind of weakness limits the applications in real-time SAR signal processing.

Here a novel algorithm is proposed by detecting the object edge under the idea that a series of pixel, which have the same gradient angle can define the edge of an object [47]. The gradient of the image indicates the gray value variation information between adjacent pixels, so it can also be used to detect the slope of a straight line. Rafael Grompone von Gioi [52] proposed a linear-time line segment detector algorithm, which can give sub-pixel accurate results and can be applied to any digital image with no parameter settings. It performs well in detecting short line segments with a low computation but cannot fit for the GMTI SAR image. Based on the principle of this method, a novel strategy is proposed to detect the slope of line in range-compressed image domain. The gradient and level-line angle of the image are the critical concepts of the method, seen in Figure 3.

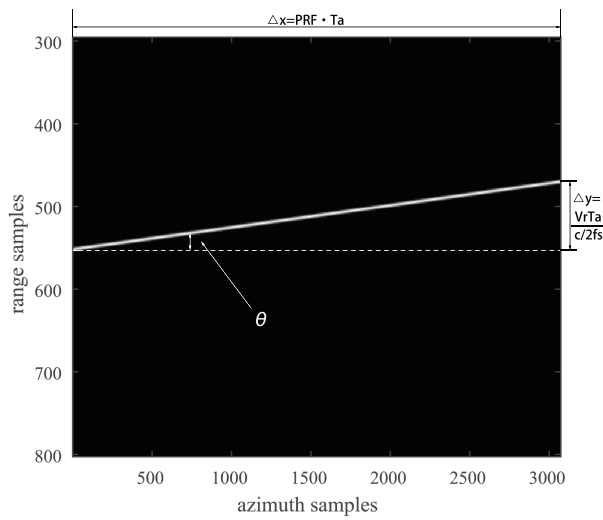


Figure 2. SAR image after range curve correction.

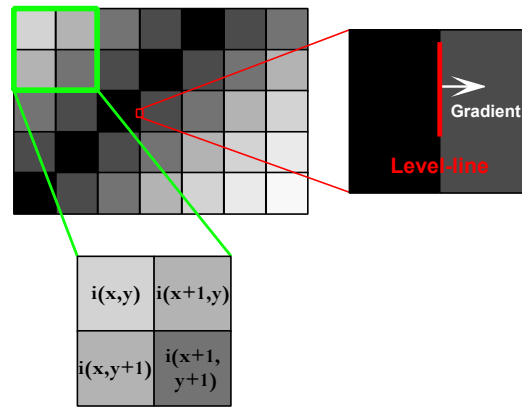


Figure 3. Gradient and level-line.

After range compressed and range curve corrected, the target trajectory can be approximated as a straight line in the image. However, the line is seriously affected by the staircase effect [52]. In order to cope with the aliasing and quantization artifacts (especially the staircase effect), an 80% image scaling is adopted, the zoom factor is the smallest image reduction that reasonably solves the staircase problem while producing almost the same result as a full-scale analysis on images without the effects of artifacts [52]. After the scaling, the number of pixels is sharply reduced to 64%. Meanwhile this operation also reduces the computing complexity to some extent.

As shown in Figure 3, a moving window of one pixel per step, called 2×2 mask, is used to calculate the image gradient. This is able to reduce the dependence of the computed gradient values in the gradient computation, which makes the method able to provide a proximal theoretical slope value of the trajectory. As is shown in Figure 3, $i(x, y)$ is the image gray value at pixel (x, y) , the image gradient can be computed with the formula as

$$\begin{aligned}
 g_x(x, y) &= \frac{i(x + 1, y) + i(x + 1, y + 1) - i(x, y) - i(x, y + 1)}{2} \\
 g_y(x, y) &= \frac{i(x, y + 1) + i(x + 1, y + 1) - i(x, y) - i(x + 1, y)}{2}
 \end{aligned}
 \tag{10}$$

Then, the gradient magnitude can be calculated by

$$G(x, y) = \sqrt{g_x^2(x, y) + g_y^2(x, y)}
 \tag{11}$$

For the edge of the line in the image, the gradient magnitude is larger than that of the adjacent pixels and the gradient direction becomes uniform. The extended direction of the edge is perpendicular to the gradient direction. By rotating the original level line angle 90 degrees counterclockwise, here the level-line angle can be computed as

$$level_line_angle = \arctan \frac{g_x(x, y)}{g_y(x, y)} \quad (12)$$

As shown in Figure 3, the edge of the line has the higher gradient magnitude, which corresponds to the more contrasted edges. From this point of view, the pixels with the highest gradient magnitude are chosen to be the seeds of the region growing algorithm. Considering the issues of computational complexity, a simple pixel pseudo-ordering method is used to institute the sorting algorithms in terms of the linear time. On the results of pseudo-ordering, the region growing algorithm is starting from the seed in the ordered list of unused pixels to form a line-support region. The adjacent pixels whose level-line angle is equal to the region angle up to a tolerance (22.5 degrees or $\pi/8$ radian, details at [52]) are added to the region. The process is repeated until no other pixel can be added to the region. While the line-support region were figured out, the enclosing rectangle description is chosen to present and judge the line-support region, as shown in Figure 4. Reference [52] uses a quiet strict and computationally complex Helmholtz Principle, it performs well in detecting short line segments but misses long lines in the image, especially in range compressed SAR image, where the trajectory is associated with all azimuth samples, as shown in Figure 2. Here a simple and effective method is introduced to replace the Helmholtz Principle. As shown in Figure 4, length to width ratio of the rectangle is used to detect a long line. For a given threshold of length to width ratio, the rectangle can be used to represent the trajectory of moving target. To estimate the slope of the trajectory, the center of the rectangle can be calculated as

$$c_x = \frac{\sum_{k=1}^{num} x_k}{num}, c_y = \frac{\sum_{k=1}^{num} y_k}{num} \quad (13)$$

where (c_x, c_y) and (x_k, y_k) are the coordinates of the rectangular center and the k th pixel in the line-support region involved by the rectangle, respectively, where num is the total number pixels contained by the rectangle. The rectangle's angle is associated with eigen value and eigen vectors of the matrix

$$M = \begin{bmatrix} m^{xx} & m^{xy} \\ m^{xy} & m^{yy} \end{bmatrix} \quad (14)$$

where

$$m^{xx} = \frac{\sum_{k=1}^{num} (x_k - c_x)^2}{num}$$

$$m^{yy} = \frac{\sum_{k=1}^{num} (y_k - c_y)^2}{num}$$

$$m^{xy} = \frac{\sum_{k=1}^{num} (x_k - c_x)(y_k - c_y)}{num}$$

Setting the eigen values as a, b ($b > a$), the corresponding eigenvectors of the bigger one is (b_1, b_2) , then the slope of the trajectory can be expressed as

$$\tan \hat{\theta} = b_2 / b_1 \quad (15)$$

Note that this method also has an excellent performance in the situation of poor SNR [52]. With the slope, the radial velocity can be well estimated. Then the RWM can be corrected by

$$H_{RWM} = \exp(j\frac{4\pi\hat{V}_r}{c}f_r t_a) \quad (16)$$

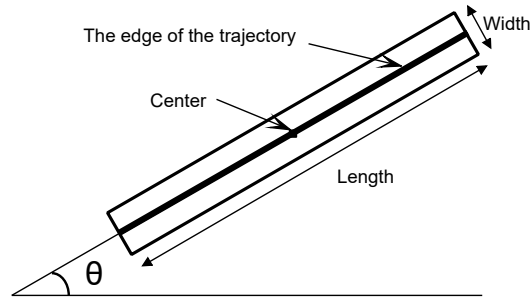


Figure 4. The edge of the trajectory is specified using a rectangle.

3.2. Along-Track Velocity Estimation

After the aforementioned operations, the radial velocity can be obtained and the response of the moving target is concentrated into a onefold range cell. Therefore, to obtain an ideal azimuth compression, the Doppler modulate rate is mainly considered in the following analysis. When RCMC and IFT are conducted, the echo signal in Equation (6) can be simplified expressed with the single variable t_a as

$$s(t_a) = A \exp(j2\pi f t_a) \exp(j\pi K^d t_a^2) \quad (17)$$

where f is the frequency with respect to Doppler centroid frequency, which is not a major concern in the following analysis. and K^d is the Doppler modulated rate, $K^d = -(2(V_a - V_x)^2)/(\lambda R_0)$. It is directly associated with the along-track velocity. In addition, for an unknown LFM signal, Time-Frequency Analysis (TFA) shows the excellent performance. The Wigner-Ville Distribution (WVD) is a well known method for TF representation. However, it has to be aware that there may be multiple moving targets located closely in the same range cell. In this case, the Azimuth Phase Modulation (APM) is in a multi-component LFM form, and the WVD is no longer useful due to its bilinearity generating cross-terms. During the implementation of Wigner-Hough Transform (WHT) and Randon-Ambiguity Transform (RAT), the rotational and searching operations are needed in the TF plane, they both suffer from a heavy computational load. The linear Fractional Fourier Transform (FrFT) can get rid of the interferences of cross-terms, but this method also brings a considerable computational load. According to [10,46], the Wigner-based methods and the FrFT methods are all failed to represent the real Doppler modulation rate. As a novel TFA technique, Lv's Distribution (LVD) can provide us a true and natural TFR in a Doppler Centroid Frequency and Chirp Rate (CFCR) domain, and cannot be disturbed by rotational, searching operations, cross-terms and any nonphysical attributes. The Doppler centroid frequency has been estimated after the application of slope estimation method as aforementioned in part Section 3.1, so only the Doppler modulation rate is considered. Detailed implementation process of the modified LVD is discussed as follows. The Parametric Symmetric Instantaneous Auto-correction Function (PSIAF) of Equation (17) can be expressed as

$$\begin{aligned} R_s^C(\tau, t_a) &= s(t_a + \frac{\tau + a}{2}) s^*(t_a + \frac{\tau + a}{2}) \\ &= A^2 \exp[j2\pi f(\tau + a)] \exp[j2\pi K^d(\tau + a)t_a] \end{aligned} \quad (18)$$

where τ is the time-lag variable, a is a constant time-delay parameter and $*$ indicates the conjugate operation. PSIAF induces a coupling between t_a and τ . The coupling can be resolved by a scaling operator

$$t_a = \frac{\tilde{t}_a}{(\tau + a)h} \quad (19)$$

where h is the scaling factor and (\tilde{t}_a) is the scaled slow-time variable. Then Equation (18) can be expressed as

$$R_S^C(\tau, \tilde{t}_a) = A^2 \exp[j2\pi f(\tau + a)] \exp[j2\pi K^d \frac{\tilde{t}_a}{h}] \quad (20)$$

when the parameters a and h are set up to 1 [19], apply Fourier transform to τ and \tilde{t}_a , the LVD representation can be therefore obtained as

$$L_s(\hat{f}, \hat{K}^d) = A^2 \exp(j2\pi f) \delta(\hat{f}) \delta(\hat{K}^d - K^d) \quad (21)$$

where $\delta(\bullet)$ denotes the Dirac delta function. \hat{f} is the estimated parameter associated with Doppler centroid frequency, \hat{K}^d is the estimated Doppler modulated rate. Then the along track velocity can be calculated by the Doppler modulate rate of the moving target as

$$\hat{V}_x = V_a - \sqrt{\frac{\lambda R_0 K^d}{2}} \quad (22)$$

Then to obtain a focused SAR image of moving target, the azimuth cubic phase can be compensated by using the same approximate principle in Equation (8) as

$$H_{cubicterm} \approx \exp(-j \frac{4\pi}{\lambda} \frac{V_r V_a^2}{2R_0^2} t_a^3) \quad (23)$$

The Doppler centroid shift can be compensated by

$$H_{f_{dc}} = \exp(j \frac{4\pi}{\lambda} V_r t_a) \quad (24)$$

The azimuth compression can be expressed as

$$H_{azimuthcompression} = \exp(-j\pi \hat{K}^d t_a^2) \quad (25)$$

The whole flowchart of the proposed algorithm is showed in Figure 5.

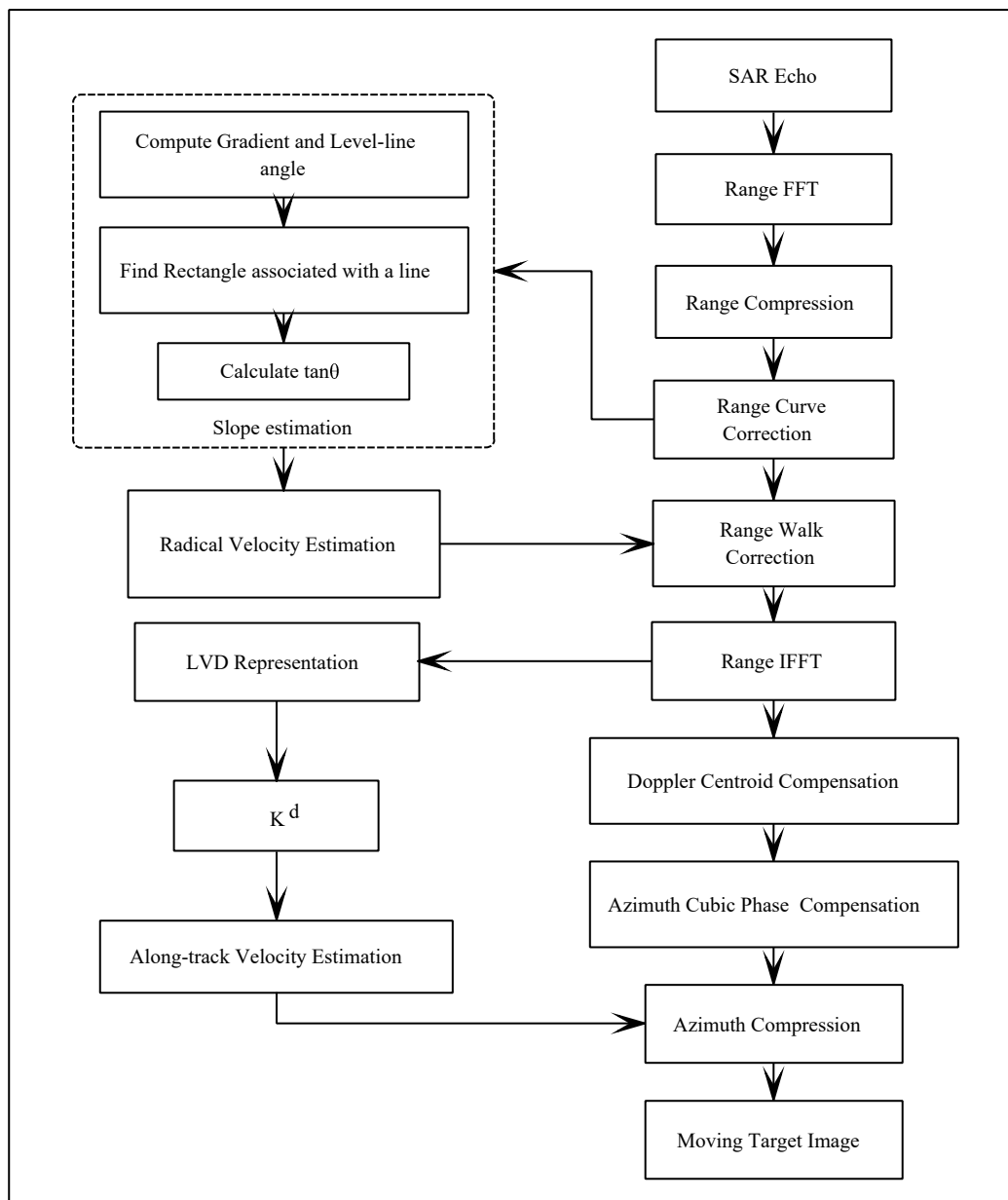


Figure 5. Flowchart of the proposed algorithm.

4. Experiments

In this section, a practical issue of the radical velocity will be discussed and a series of experiments is devised to verify the performance of the proposed algorithm.

4.1. The Analysis of Parameters Error

Recall Equation (8), the estimation of radical velocity is highly significant for the RWMC and the term, $PRFC/2f_c$ has a very large magnitude, so that the accuracy of slope is a vital factor to acquire a well focused image. As shown in Table 1, it can be seen that for a given radial velocity of 25 m/s, the estimated velocity is more accurate for the smaller searching range. Likewise, Figure 6 shows the imaging result under different searching ranges. It is evident that the smaller the searching step, the greater the imaging quality. Therefore, both the numerical results shown in Table 1 and Figure 6 demonstrate that the estimation accuracy of the slope has the significant effect on the focusing of

moving target image. In other words, due to the existence of the estimation of slope error, the target cannot be well focused in the final image.

Table 1. A comparison of moving target imaging with different searching ranges.

V_{real}	$V_{estimate}$			
	searching ranges			
25 m/s	1°	0.1°	0.01°	0.001°
	32.7382214 m/s	26.18674612 m/s	25.20426081 m/s	25.02414457 m/s

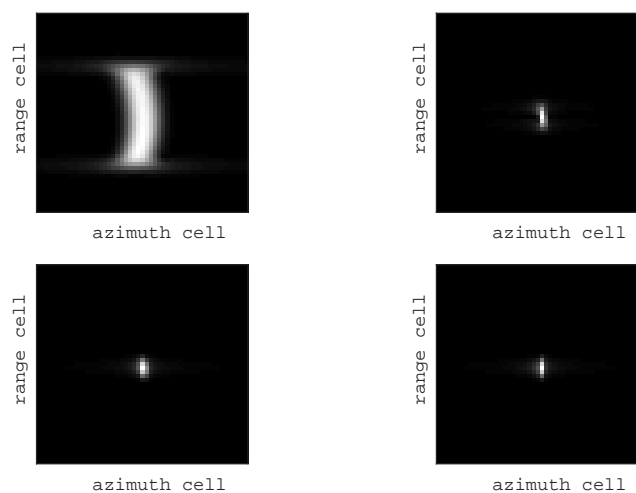


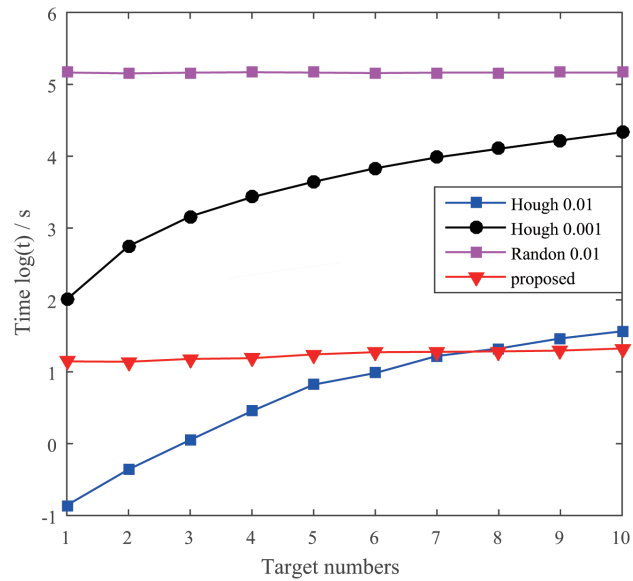
Figure 6. A comparison of moving target imaging with different searching ranges.

4.2. Performance Comparison

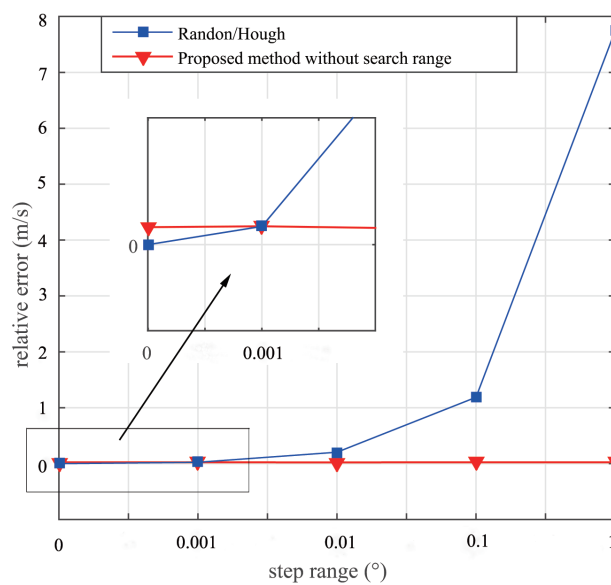
The following numerical results are obtained by simulation with the parameters presented in Table 2. It is well-known that HT has a better performance than RT in term of computation complexity. From this point of view, the following performance comparison focuses on the HT and the proposed algorithm. Figure 7a shows the computing time versus the number of moving targets for HT and the proposed algorithm, since the computing time is directly related to the complexity of algorithm. It can be seen that the proposed algorithm has almost a constant computing time irrespective of the number of moving target increasing. In contrast, the computing time for the HT algorithm is exponentially increasing as the number of the moving targets increases, especially for a high accuracy of 0.001, which gives to a reasonable good image focusing. The reason for the proposed algorithm to have significant performance in terms of computing time is that the proposed algorithm is able to provide a slope close to its theoretical value. Furthermore, when the number of moving targets is more than 7, the proposed algorithm shows superiority to HT at an accuracy of 0.01. Figure 7b shows the relative error of radial velocity for RT/HT and the proposed algorithm. It can be seen that the proposed algorithm has excellent precise result regardless the search range changes. This means that the proposed algorithm does not need to prior set up the search range. In contrast, both RT and HT need to set up the search range in order to achieve a good estimation on target moving velocity. From Figure 7a, it can be seen that the computing time is presented in *log* scale, so that when RT or HT changes its search range from 0.01 to 0.001, the required computing time increases exponentially.

Table 2. Simulation Parameters.

Parameter Name	Value
carrier Frequency	9.6 GHz
pulse time width	4 μ s
pulse bandwidth	80 MHz
nearest slant range	7500 m
pulse repetition frequency	1000 Hz
platform velocity	150 m/s



(a)



(b)

Figure 7. Performance comparison: (a) Computational load of different methods; (b) Relative error comparison of radial velocity.

4.3. Simulated Data Processing

Figure 8 shows a simulation model of single channel SAR system of 4 targets using the same parameters presented in Table 2, where *S* represents a stationary target, *M1*, *M2*, *M3* represent moving targets with different velocities, respectively. All the moving and stationary targets are supposed to be isotropic point targets in the scene. In Table 3, V_x (V_r) and \hat{V}_x (\hat{V}_r) represent the given along-track velocity (the given radial velocity) and the estimated along-track velocity (the estimated radial velocity), respectively. To incorporate simulated moving targets, the initial positions in range-azimuth domain for these 4 targets are shown in Figure 8. In the simulation, after rang walk corrected for the 3 moving targets, LVD representation is used to estimate the Doppler modulation rate. The obtained result is shown in Figure 9. The SAR image of moving targets using the proposed algorithm is given in Figure 10, in which the initial position of the moving target is presented by cross symbol. Due to the motion of the target, the moving target response is displaced and defocused that is revealed by square symbol. The relocated and refocused moving target by the proposed algorithm is presented by circle symbol. Figure 11a,b illustrate the target contour image for the moving target *M2* of defocused after RCMC and refocused by LVD, respectively. To have a more intuitive demonstration, Figure 12 shows the comparison of azimuth responses of *M2* corresponding to that in Figure 11.

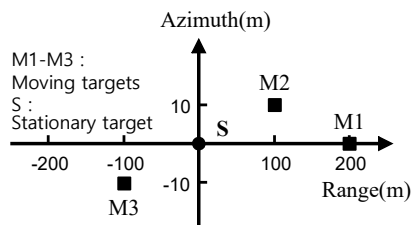


Figure 8. Simulated target ground truth.

Table 3. Simulated and estimated target velocity.

	V_r (m/s)	V_x (m/s)	\hat{V}_r (m/s)	\hat{V}_x (m/s)
M1	10	10	9.9975	10.0123
M2	25	5	24.9964	5.0215
M3	10	3	9.9973	3.0118

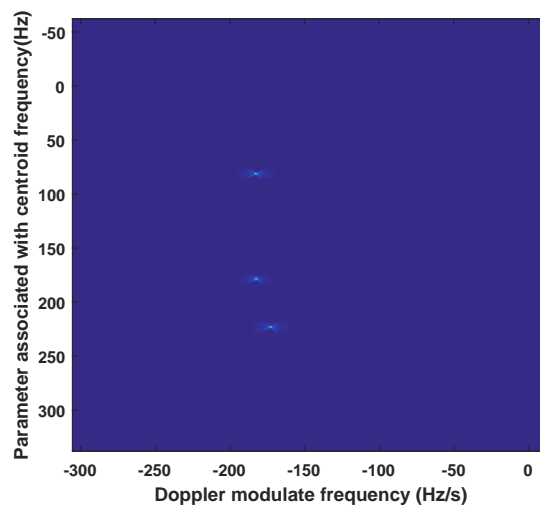


Figure 9. LVD representation.

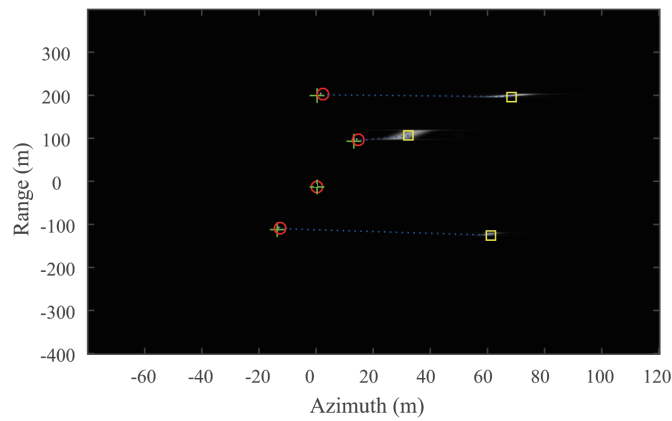


Figure 10. SAR moving target imaging result. The initial position of the moving target is presented by cross symbol. The displaced and defocused target is presented by square symbol. The relocated and refocused moving target using the proposed algorithm is presented by circle symbol.

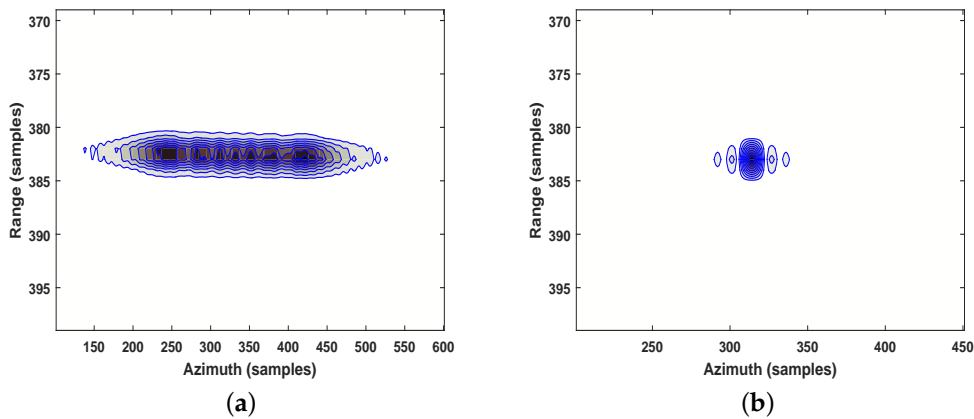


Figure 11. M2 contour image: (a) Range focused image after range walk correction, Doppler centroid shift compensation and the cubic term compensation; (b) Final focused image.

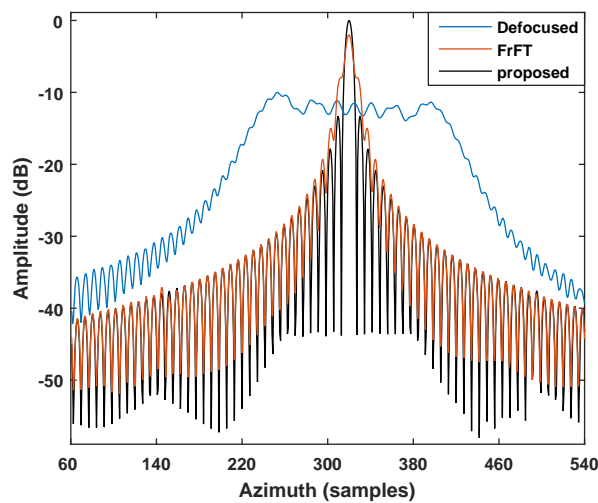


Figure 12. Azimuth responses of defocused and refocused of M2. (Blue line) Defocused target response. (Brown line) refocused target response based on FrFT representation. (Solid line) Refocused target response based on LVD representation.

5. Conclusions

This paper presents a novel SAR imagery algorithm SDLVD for ground moving targets based on the slope detection strategy combined with LVD. The novelty is the solution of the ambiguity problem and relevant heavy computing load. This research consists of two main focuses. The first focus is a new high-efficiency slope detection strategy based on the concept of gradient and level-line angle. This strategy is able to achieve accurate slope estimation and save significant computing. For example, as shown in Figure 7, when there are seven moving targets in the observed scene, the velocity estimation error rate of using the proposed algorithm is approximately equal to the conventional RT/HT algorithm with a searching range 0.001. However, the proposed algorithm can save up to 34 s of computing time comparing to RT/HT algorithm. The second focus is a novel time-frequency representation method, known as LVD, to represent a true and natural doppler chirp rate for multiple moving targets in a doppler centroid frequency and chirp rate domain. This can be evidenced by the capability of refocusing the multiple moving targets as shown in Figures 9 and 10. Furthermore, as shown in Figure 12, the refocused target responses using LVD representation have narrower main lobes and lower side lobes comparing to the conventional FrFT approach.

In summary, the proposed algorithm can be used for real-time SAR remote sensing system due to the high accurate velocity estimation, less computing time and refocused target responses. The future work will test the proposed algorithm on SAR platform, especially on the UAV borne SAR platform.

Author Contributions: The manuscript is written by S.H. under the guidance of Y.Z., J.W. and L.Z. The related research work was carried by S.H. including analysis and simulation. J.W. and Y.Z. and L.Z. have played the supporting role in the theoretical modeling and simulation methodology through seminars and discussions. The other co-authors have made their contributions through the discussions. The manuscript was finally revised by L.Z.

Acknowledgments: This work was partially supported by Project of Shandong Province Higher Educational Science and Technology Program under Grand No. J16LN21 and the Shandong Province University Science and Technology Project No. J17KA082.

Conflicts of Interest: The authors declare no conflict of interest.

References

1. Yang, J.; Liu, C.; Wang, Y. Imaging and Parameter Estimation of Fast-Moving Targets With Single-Antenna SAR. *IEEE Geosci. Remote Sens. Lett.* **2013**, *11*, 529–533. [[CrossRef](#)]
2. Jin, T.; Qiu, X.; Hu, D.; Ding, C. An ml-based radial velocity estimation algorithm for moving targets in spaceborne high-resolution and wide-swath sar systems. *Remote Sens.* **2017**, *9*, 404. [[CrossRef](#)]
3. Zhu, S.; Liao, G.; Qu, Y.; Zhou, Z.; Liu, X. Ground Moving Targets Imaging Algorithm for Synthetic Aperture Radar. *IEEE Trans. Geosci. Remote Sens.* **2010**, *49*, 462–477. [[CrossRef](#)]
4. Gao, G.; Shi, G. The CFAR Detection of Ground Moving Targets Based on a Joint Metric of SAR Interferogram's Magnitude and Phase. *IEEE Trans. Geosci. Remote Sens.* **2012**, *50*, 3618–3624. [[CrossRef](#)]
5. Gao, G.; Shi, G.; Yang, L.; Zhou, S. Moving target detection based on the spreading characteristics of SAR interferograms in the magnitude-phase plane. *IEEE Trans. Remote Sens.* **2015**, *7*, 1836–1854. [[CrossRef](#)]
6. Sun, G.; Xing, M.; Xia, X.G.; Wu, Y.; Bao, Z. Robust Ground Moving-Target Imaging Using Deramp-Keystone Processing. *IEEE Trans. Geosci. Remote Sens.* **2013**, *51*, 966–982. [[CrossRef](#)]
7. Hansen, R.E.; Sabo, T.O.; Synnes, S.A.; Lorentzen, O.E. Synthetic aperture sonar interferometry for detailed seabed mapping: Performance considerations. *J. Acoust. Soc. Am.* **2017**, *141*, 4004, doi:10.1121/1.4989186. [[CrossRef](#)]
8. Hooper, A. A multi-temporal InSAR method incorporating both persistent scatterer and small baseline approaches. *Geophys. Res. Lett.* **2008**, *35*. [[CrossRef](#)]
9. Plank, S.; Martinis, S.; Twele, A. Rapid Landslide Mapping by Means of Post-Event Polarimetric SAR Imagery. In Proceedings of the Conference on Living Planet Symposium, Prague, Czech Republic, 9–13 May 2016; Volume 740, p. 307.
10. Yang, L.; Bi, G.; Xing, M.; Zhang, L. Airborne sar moving target signatures and imagery based on LVD. *IEEE Trans. Geosci. Remote Sens.* **2015**, *53*, 5958–5971. [[CrossRef](#)]

11. Dragosevic, M.V.; Burwash, W.; Shen, C. Detection and estimation with radarsat-2 moving-object detection experiment modes. *IEEE Trans. Geosci. Remote Sens.* **2012**, *50*, 3527–3543. [[CrossRef](#)]
12. Sikaneta, I.C.; Chouinard, J.Y. Eigendecomposition of the multi-channel covariance matrix with applications to SAR-GMTI. *Signal Process.* **2004**, *84*, 1501–1535. [[CrossRef](#)]
13. Baumgartner, S.V.; Krieger, G. Experimental Verification of High-Resolution Wide-Swath Moving Target Indication. In Proceedings of the 9th European Conference on Synthetic Aperture Radar (EUSAR), Nuremberg, Germany, 23–26 April 2008; pp. 437–440.
14. Yang, T.L.; Wang, Y. A novel algorithm to estimate moving target velocity for a spaceborne HRWS SAR/GMTI system. In Proceedings of the 2010 IEEE International Geoscience and Remote Sensing Symposium (IGARSS), Beijing, China, 10–15 July 2016; pp. 3242–3245.
15. Wang, X.Y.; Wang, R.; Li, N.; Zhou, C. A velocity estimation method of moving target for HRWS SAR. In Proceedings of the 2010 IEEE International Geoscience and Remote Sensing Symposium (IGARSS), Beijing, China, 10–15 July 2016; pp. 6819–6822.
16. Zhang, S.X.; Xing, M.D.; Xia, X.G.; Guo, R.; Liu, Y.Y.; Bao, Z. Robust clutter suppression and moving target imaging approach for multichannel in azimuth high-resolution and wide-swath synthetic aperture radar. *IEEE Trans. Geosci. Remote Sens.* **2014**, *53*, 687–709. [[CrossRef](#)]
17. Wu, Q.; Xing, M.; Qiu, C.; Liu, B.; Bao, Z.; Yeo, T.S. Motion parameter estimation in the sar system with low prf sampling. *IEEE Geosci. Remote Sens. Lett.* **2010**, *7*, 450–454. [[CrossRef](#)]
18. Zhang, S.X.; Xing, M.D.; Xia, X.G.; Guo, R.; Liu, Y.Y.; Bao, Z. A novel moving target imaging algorithm for hrws sar based on local maximum-likelihood minimum entropy. *IEEE Trans. Geosci. Remote Sens.* **2014**, *52*, 5333–5348. [[CrossRef](#)]
19. Wang, L.B.; Wang, D.W.; Li, J.J.; Xu, J.; Xie, C.; Wang, L. Ground moving target detection and imaging using a virtual multichannel scheme in hrws mode. *IEEE Trans. Geosci. Remote Sens.* **2016**, *54*, 5028–5043. [[CrossRef](#)]
20. Jao, J.K. Theory of synthetic aperture radar imaging of a moving target. *IEEE Trans. Geosci. Remote Sens.* **2001**, *39*, 1984–1992.
21. Arii, M. Efficient motion compensation of a moving object on sar imagery based on velocity correlation function. *IEEE Trans. Geosci. Remote Sens.* **2014**, *52*, 936–946. [[CrossRef](#)]
22. Budillon, A.; Pascazio, V.; Schirinzi, G. Moving targets detection and velocity estimation via multi-channel along-track interferometry. In Proceedings of the 2005 IEEE International Geoscience and Remote Sensing Symposium (IGARSS), Seoul, Korea, 25–29 July 2005; pp. 2672–2675.
23. Wang, H.S.C. Mainlobe clutter cancellation by DPCA for space-based radars. In Proceedings of the IEEE Aerospace Applications Conference, Crested Butte, CO, USA, 3–8 February 1991.
24. Hou, Y.; Wang, J.; Liu, X.; Wang, K.; Gao, Y. An automatic SAR-GMTI algorithm based on DPCA. In Proceedings of the 2014 IEEE International Geoscience and Remote Sensing Symposium (IGARSS), Quebec City, QC, Canada, 13–18 July 2014; pp. 592–595.
25. Vu, V.T.; Sjogren, T.K.; Pettersson, M.I. Space time adaptive processing for moving target detection and imaging in bistatic SAR. In Proceedings of the 2011 IEEE International Geoscience and Remote Sensing Symposium (IGARSS), Sendai, Japan, 31 July–5 August 2014; pp. 592–595.
26. Cerutti-Maori, D.; Sikaneta, I. Optimum GMTI processing for space-based SAR/GMTI systems-theoretical derivation. In Proceedings of the EUSAR, Aachen, Germany, 7–10 June 2010; pp. 1–4.
27. Raney, R.K. Synthetic aperture imaging radar and moving targets. *IEEE Trans. Aerosp. Electron. Syst.* **1971**, *7*, 499–505. [[CrossRef](#)]
28. Guo, B.; Vu, D.; Xu, L.; Xue, M.; Li, J. Ground moving target indication via multichannel airborne SAR. *IEEE Trans. Geosci. Remote Sens.* **2011**, *49*, 3753–3764. [[CrossRef](#)]
29. Zhang, Y.; Zhang, X.; Li, H.; Wang, Z.; Zhuang, Y. Detection and imaging of moving objects with multichannel SAR system. In Proceedings of the 2015 IEEE International Geoscience and Remote Sensing Symposium (IGARSS), Milan, Italy, 26–31 July 2015; pp. 2417–2420.
30. Wang, G.; Xia, X.G.; Chen, V.C.; Fielder, R.L. Detection, location, and imaging of fast moving targets using multifrequency antenna array SAR. *SPIE Proc.* **2004**, *40*, 345–355.
31. Tan, K.; Li, W. Imaging and parameter estimating for fast moving targets in airborne SAR. *IEEE Trans. Comput. Imaging* **2017**, *3*, 126–140. [[CrossRef](#)]

32. Perry, R.P.; Dipietro, R.C.; Fante, R.L. SAR imaging of moving targets. *IEEE Trans. Aerosp. Electr. Syst.* **1999**, *35*, 188–200. [[CrossRef](#)]
33. Zhou, F.; Wu, R.; Xing, M.; Bao, Z. Approach for single channel sar ground moving target imaging and motion parameter estimation. *IET Radar Sonar Navig.* **2007**, *1*, 59–66. [[CrossRef](#)]
34. Li, G.; Xia, X.G.; Peng, Y.N. Doppler keystone transform: An approach suitable for parallel implementation of sar moving target imaging. *IEEE Geosci. Remote Sens. Lett.* **2008**, *5*, 573–577. [[CrossRef](#)]
35. Yang, J.; Huang, X.; Tian, J.; Thompson, J.; Zhou, Z. New approach for sar imaging of ground moving targets based on a keystone transform. *IEEE Geosci. Remote Sens. Lett.* **2011**, *8*, 829–833.
36. Zhu, D.; Li, Y.; Zhu, Z. A keystone transform without interpolation for sar ground moving-target imaging. *IEEE Geosci. Remote Sens. Lett.* **2007**, *4*, 18–22. [[CrossRef](#)]
37. Kong, Y.K.; Cho, B.L.; Kim, Y.S. Ambiguity-free doppler centroid estimation technique for airborne sar using the radon transform. *IEEE Trans. Geosci. Remote Sens.* **2005**, *43*, 715–721. [[CrossRef](#)]
38. Xu, R.; Zhang, D.; Hu, D.; Qiu, X.; Ding, C. A novel motion parameter estimation algorithm of fast moving targets via single-antenna airborne SAR system. *IEEE Geosci. Remote Sens. Lett.* **2012**, *9*, 920–924.
39. Zhu, S.; Liao, G.; Qu, Y.; Liu, X.; Zhou, Z. A new slant-range velocity ambiguity resolving approach of fast moving targets for SAR system. *IEEE Trans. Geosci. Remote Sens.* **2009**, *48*, 432–451.
40. Cumming, I.G.; Li, S. Improved slope estimation for sar doppler ambiguity resolution. *IEEE Trans. Geosci. Remote Sens.* **2006**, *44*, 707–718. [[CrossRef](#)]
41. Yang, J.; Liu, C.; Wang, Y. Detection and imaging of ground moving targets with real SAR data. *IEEE Trans. Geosci. Remote Sens.* **2015**, *53*, 920–932. [[CrossRef](#)]
42. Hou, L.; Song, H.; Zheng, M.; Wang, W. Fast moving target imaging and motion parameters estimation based on radon transform and bi-directional approach. *IET Radar Sonar Navig.* **2016**, *10*, 1013–1023. [[CrossRef](#)]
43. Li, W.; Yang, J.; Huang, Y. Improved doppler parameter estimation of squint SAR based on slope detection. *Int. J. Remote Sens.* **2014**, *35*, 1417–1431. [[CrossRef](#)]
44. Xia, X.G.; Chen, V.C. A quantitative snr analysis for the pseudo Wigner-Ville distribution. *IEEE Trans. Signal Process.* **1999**, *47*, 2891–2894.
45. Almeida, L.B. The fractional fourier transform and time-frequency representations. *IEEE Trans. Signal Process.* **1994**, *42*, 3084–3091. [[CrossRef](#)]
46. Lv, X.; Bi, G.; Wan, C.; Xing, M. Lv's distribution: Principle, implementation, properties, and performance. *IEEE Trans. Signal Process.* **2011**, *59*, 3576–3591. [[CrossRef](#)]
47. Gioi, R.G.V.; Jakubowicz, J.; Morel, J.M.; Randall, G. On straight line segment detection. *J. Math. Imaging Vis.* **2008**, *59*, 3576–3591.
48. Yu, W.; Su, W.; Gu, H. Fast method for radar maneuvering target detection and motion parameter estimation. *Multidimens. Syst. Signal Process.* **2017**, *4*, 1–15. [[CrossRef](#)]
49. Yang, L.; Zhao, L.; Bi, G.; Zhang, L. Sar ground moving target imaging algorithm based on parametric and dynamic sparse bayesian learning. *IEEE Trans. Geosci. Remote Sens.* **2016**, *54*, 2254–2267. [[CrossRef](#)]
50. Yu, W.; Su, W.; Gu, H. Ground moving target motion parameter estimation using radon modified lv's distribution. *Digit. Signal Process.* **2017**, *69*, 212–223. [[CrossRef](#)]
51. Yu, W.; Su, W.; Gu, H. Ground maneuvering target detection based on discrete polynomial-phase transform and Lv's distribution. *Signal Process.* **2018**, *144*, 364–372. [[CrossRef](#)]
52. Gioi, R.G.V.; Jakubowicz, J.; Morel, J.M.; Randall, G. Lsd: A line segment detector. *Image Process. Line* **2012**, *2*, 35–55. [[CrossRef](#)]

